

Evaluation of a Canonical Image Representation for Sidescan Sonar

WeiQi Xu weiqi@kth.se

KTH - Royal Institute of Technology
Stockholm, Sweden

Li Ling liling@kth.se

KTH - Royal Institute of Technology
Stockholm, Sweden

Yiping Xie yipingx@kth.se

KTH - Royal Institute of Technology
Stockholm, Sweden

Jun Zhang juzhang@kth.se

KTH - Royal Institute of Technology
Stockholm, Sweden

John Folkesson johnf@kth.se

KTH - Royal Institute of Technology
Stockholm, Sweden

Abstract—Acoustic sensors play an important role in autonomous underwater vehicles (AUVs). Sidescan sonar (SSS) detects a wide range and provides photo-realistic images in high resolution. However, SSS projects the 3D seafloor to 2D images, which are distorted by the AUV’s altitude, target’s range and sensor’s resolution. As a result, the same physical area can show significant visual differences in SSS images from different survey lines, causing difficulties in tasks such as pixel correspondence and template matching. In this paper, a canonical transformation method consisting of intensity correction and slant range correction is proposed to decrease the above distortion. The intensity correction includes beam pattern correction and incident angle correction using three different Lambertian laws (\cos , \cos^2 , \cot), whereas the slant range correction removes the nadir zone and projects the position of SSS elements into equally horizontally spaced, view-point independent bins. The proposed method is evaluated on real data collected by a HUGIN AUV, with manually-annotated pixel correspondence as ground truth reference. Experimental results on patch pairs compare similarity measures and keypoint descriptor matching. The results show that the canonical transformation can improve the patch similarity, as well as SIFT descriptor matching accuracy in different images where the same physical area was ensonified.

I. INTRODUCTION

Autonomous underwater vehicles (AUVs) equipped with sonars allow us to collect acoustic returns from the seabed at closer distances, thus providing data with higher resolution compared to surface vessels. However, without GPS, the pose estimate of the AUVs is prone to accumulative drift. Accurate pose estimation is of paramount importance when exploring or inspecting underwater environments with AUVs, since the oceanographic data collected need to be accurately geo-referenced. Acoustic ranging systems such as ultra short baseline systems (USBL) are often pre-installed on-site to help reduce the AUV’s position estimates in commercial surveys. However, such systems are costly and time-consuming to deploy, and significantly restrict the AUV’s survey area.

Simultaneous localization and mapping (SLAM) [1] offers a more flexible and cost-effective way of reducing drift in vehicle pose estimates. In underwater SLAM, the most frequently used sensors include underwater camera, multi-beam echosounder (MBES), and sidescan sonar (SSS) [2]–

[4]. Compared to cameras, SSS allows for sensing of much longer range. Compared to MBES, SSS can often have a higher resolution and is lower cost and easier to mount on an AUV. Using SSS images for pose correction in any SLAM framework requires successful loop closure detection, or the detection of overlap in SSS images collected from different survey lines. However, detecting matching feature pairs in SSS for loop closures is challenging, since the features on the seabed will appear differently in the SSS images collected from different distances and angles. The pixel intensity (due to reflection and transmission) and resolution (due to geometric distortions) of SSS image are affected by multiple factors, including the vehicle’s altitude, velocity, the sensor properties as well as the physical properties of the ensonified seafloor [5], [6]. As a result, SSS images of the same physical area will differ from one another, necessitating intensity and range correction prior to the feature correspondence matching tasks. In particular, an image patch will be distorted compared to an orthographic projection of the ensonified region and will vary in intensity as a function of the sonar position, see Fig. 1 (left).

In this paper, we present a method capable of transforming SSS images from different survey lines into a canonical representation where the affect of the aforementioned SSS distortions is reduced. The proposed method extends previously proposed SSS normalization algorithms in two ways: 1) Intensity corrections using three different relationships with incidence angles are compared. 2) The proposed algorithm allows for an arbitrary size of pixel resolution, making it easier to compare SSS images across sensors and settings. Such a canonical representation of SSS images allows us to create datasets from different surveys, which is essential for learning-based approach to tackle the data association problem in SSS SLAM.

To validate the effectiveness of our proposed canonical transformation, SSS images of the *same* physical area taken from multiple survey lines are used. Compared to the raw SSS images, we show experimentally that SSS images in the canonical representation obtain significantly higher image similarity scores and better descriptor matching accuracy. In

ssh171-patch0 ssh173-patch0 ssh171-patch0 ssh173-patch0

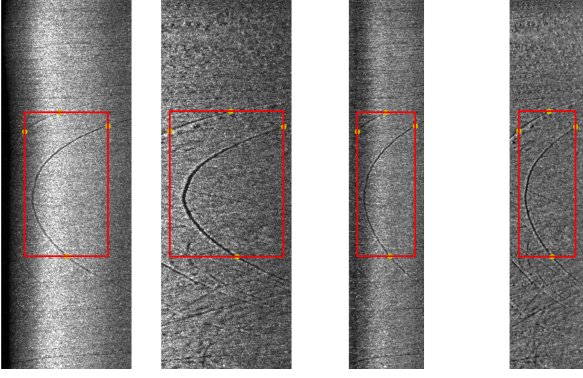


Fig. 1: The same physical seafloor area in SSS patches extracted from different survey lines. The left two patches are extracted from raw images, and the right two patches are extracted from canonical images generated using \cos^2 Lambertian law. The red rectangle highlights the same physical pattern across all images.

summary, the contributions of this work are:

- 1) Presents a canonical transformation method with detailed comparison of three Lambertian laws, and a sensor independent slant range correction algorithm which allows arbitrary ground range resolution.
- 2) Conducts extensive experiments on real data with annotated keypoints as ground truth reference, using metrics of correlation measure, histogram distance and descriptor matching, to prove the effectiveness of canonical representation of SSS image.
- 3) Demonstrates results of improvements in canonical images over raw images in patch similarity and descriptor matching accuracy, showing great potentials in application to downstream tasks such as SSS image mosaicking and SLAM, etc.

II. RELATED WORK

Sidescan sonar images are affected by both geometric and intensity distortions. Geometric distortions can be addressed by slant range correction and corrections with respect to sonar's altitudes and AUV's speed. Intensity distortion can be corrected by accounting for sonar's beam pattern, incidence angle variations and seabed sediments variations.

One of early work is Cobra et al. [7], where they only use the sonar images themselves to estimate and correct geometric distortions introduced by motion instabilities of the towfish, whose stability is much worse than AUVs. Chavez *et al.* [8] give a overview on how to apply both geometric distortions and intensity distortions to create a mosaic from multiple sidescan images. Burguera and Oliver [6], [9] propose a detailed SSS correction model under the flat sea floor assumption. The model includes intensity correction procedure with a physical ensonification intensity model to compensate the sonar's beam pattern, and a slant range correction to remove geometric distortions. The slant range correction is sensor

dependant, since the ground range resolution is chosen to be the same as the slant range resolution, making the algorithm a simple linear interpolation between two corresponding adjacent bins. Zhao *et al.* [10] propose a new intensity correction method addressing the variations of the seabed sediment with an unsupervised sediment classification algorithm.

The time-varying gain (TVG) is usually applied to the sidescan returned echos onboard during the mission to compensate the intensity variations due to the range effect. However, the exact parameters of the TVG are usually unavailable. Capus *et al.* [11] propose a method to estimate the range-dependent residual TVG effects together with the angle-dependent beam pattern, which reduces some artefacts in sidescan images.

The distortion estimation and correction are usually the pre-processing steps for specific applications such as mosaicking [12], mapping [9], localization [13] and SLAM [14]. Burguera and Bonin-Font applied the correction methods in [9] to remove the artifacts and distortions in the SSS images before feeding them to a CNN for segmentation [15]. In this paper, we demonstrate the effectiveness of canonical transformation on reducing geometric and intensity distortions. The proposed method can be used as a pre-processing step for feature matching [16], [17] and loop closure detection [18] in SLAM.

III. CANONICAL TRANSFORMATION OF SSS

Due to the variability and distortions of SSS images mentioned in Section I, works that perform automation on SSS images normally include a pre-processing step. In general, this pre-processing consists of intensity correction and slant range correction [5], [6], [9], [19], and our proposed method follows the same schema.

1) *Intensity Correction:* Intensity correction aims to normalize the intensities across the image. The goal is to have a perfectly flat/horizontal seafloor producing a perfectly uniform intensity. The actual image will then only show differences due to deviations from that assumption. To perform such correction, the SSS backscatter intensity is usually modelled using the *Lambertian* model [6], [19]:

$$I(p) = K\Phi(p)R(p)|\cos(\theta(p))|, \quad (1)$$

where K is the normalization constant, p is the reflection point, and $\Phi(p)$, $R(p)$, $\theta(p)$ are the beam pattern, reflectivity and incident angle at point p , respectively. We model the beam pattern as the theoretical model of a linear array with a large number of elements, similar as in [20]:

$$\Phi(\phi(p)) = \left(\frac{k_\phi \cdot \sin(\phi - \phi_0)}{\sin(k_\phi \cdot \sin(\phi - \phi_0))} \right)^4, \quad (2)$$

where $k_\phi = 2.78$ for a 3 dB beam width of 60° and $\phi_0 = 30^\circ$ is the angle of depression that the sonar is mounted. The value of both beam width and ϕ_0 are sensor dependent.

An intensity \tilde{I} free from incidence angle is thereby achieved using Equation 3:

$$\tilde{I}(p) = \frac{I(p) \sec(\theta(p))}{\Phi(\phi(p))}. \quad (3)$$

The $\sec(\theta(p))$ implies that the backscatter intensity is proportional to the cosine of the incidence angle. However, cosine square (\cos^2) [21], [22] and cotangent (\cot) [23] relationships have also been suggested. In this work, we explore all three relationships for the intensity correction module and compare the resulting canonical representations using similarity scores and descriptor matching accuracies. The evaluation results are found in Section IV.

2) *Sensor Independent Slant Range Correction*: This correction adjusts for the varying projection of the sidescan pixels on the (assumed) horizontal seafloor. The problem of geometric distortion in raw SSS images is visualized in Fig. 2. Although each consecutive bin/pixel is sampled at the same slant range resolution Δr , the resulting ground range resolution of d_i and d_j are different. As evident in Fig. 2, bins sampled with smaller incidence angle θ (i.e. closer to the sonar head) will cover larger physical area compared to bins sampled with larger incidence angle.

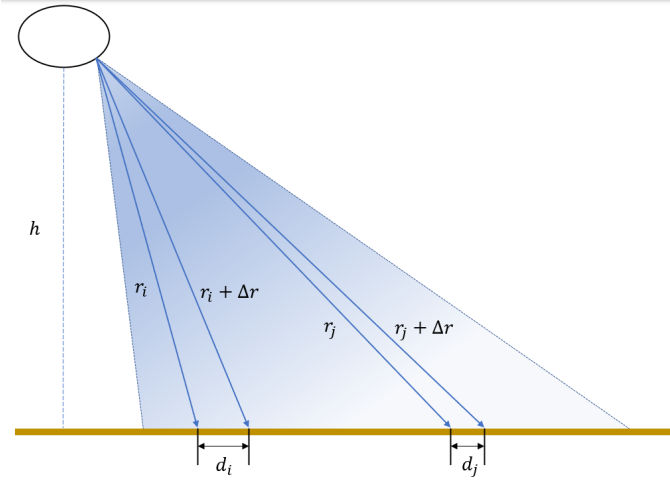


Fig. 2: An intuitive comparison of ground range bin sizes at different slant ranges. With the same slant range resolution Δr , the effective ground range resolution increases as we move away from the sonar head.

In our method, we first project all the sonar intensities to the assumed horizontal seafloor. Then we average and interpolate them to fixed horizontal size pixels. The interpolated intensities can be computed as the weighted sum of original intensities:

$$\bar{I}_i = \sum_j w_{ij} \tilde{I}_j, \quad (4)$$

where \bar{I}_i is the i th bin in swath after canonical transformation, \tilde{I}_j is the j th bin after intensity correction, and w_{ij} is the weight contributed to bin \bar{I}_i by \tilde{I}_j , which is proportional to the corresponding distance of the j th bin along the horizontal line covered by the i th bin after interpolation. Here w_{ij} is normalized so that $\sum_j w_{ij} = 1$.

A concrete schema is shown in Fig. 3, where $r_{g,j}$ and $\bar{r}_{g,i}$ are the ground range before and after uniformly spaced

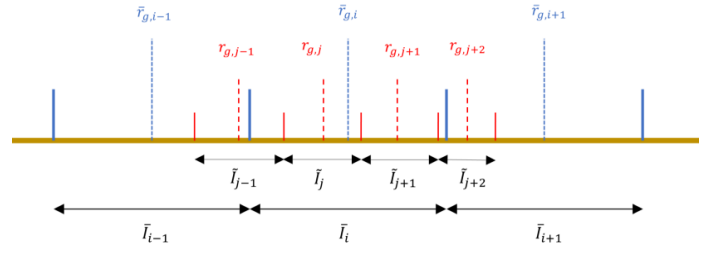


Fig. 3: Interpolation in uniform ground range. The red solid vertical lines are the original points where the sidescan bin range hits the horizontal seafloor and the red dashed lines are the midpoints. The blue solid vertical lines are the evenly spaced ground range points and the blue dashed vertical lines are the midpoints [24].

ing, respectively. The fixed size \bar{I}_i is the weighted sum of $\tilde{I}_{j-1}, \tilde{I}_j, \tilde{I}_{j+1}, \tilde{I}_{j+2}$:

$$\begin{aligned} \bar{I}_i = & \left[\left(\frac{r_{g,j-1} + r_{g,j}}{2} \right) - \left(\bar{r}_{g,i} - \frac{\delta_g}{2} \right) \right] \tilde{I}_{j-1} \\ & + \left(\frac{r_{g,j+1} - r_{g,j-1}}{2} \right) \tilde{I}_j + \left(\frac{r_{g,j+2} - r_{g,j}}{2} \right) \tilde{I}_{j+1} \\ & + \left[\left(\bar{r}_{g,i} + \frac{\delta_g}{2} \right) - \left(\frac{r_{g,j+2} + r_{g,j+1}}{2} \right) \right] \tilde{I}_{j+2}. \end{aligned} \quad (5)$$

The pseudo code of the slant correction algorithm for one ping is given in Algorithm 1.

Algorithm 1 Slant range correction for one ping

Input: Intensity corrected ping \tilde{I} of length m

for all $i = 1, \dots, m$ **do**

$$j_1 = \arg \max_j [(\bar{r}_{g,i} - \frac{\delta_g}{2}) \in N(j)]$$

$$j_n = \arg \min_j [(\bar{r}_{g,i} + \frac{\delta_g}{2}) \in N(j)]$$

$$w_{ij_0} = \frac{r_{g,j_0} + r_{g,j_0+1}}{2} - \left(\bar{r}_{g,i} - \frac{\delta_g}{2} \right)$$

$$w_{ij_n} = \left(\bar{r}_{g,i} + \frac{\delta_g}{2} \right) - \frac{r_{g,j_n} + r_{g,j_n+1}}{2}$$

for all $j = j_0 + 1, \dots, j_n - 1$ **do**

$$w_{ij} = \frac{r_{g,j+1} - r_{g,j-1}}{2}$$

end for

$$\text{Normalize } [w_{ij_1}, \dots, w_{ij_n}]$$

$$\bar{I}_i = \sum_j w_{ij} \tilde{I}_j$$

end for

Given the altitude h and maximum slant range $r_{s,\max}$ of one SSS ping, we project all the sonar elements to the assumed horizontal seafloor starting from $\theta_0 = 30^\circ$ incidence angle, which gives us the ground range from $r_{g,\min} = h \tan(\theta_0)$ to $r_{g,\max} = \sqrt{r_{s,\max}^2 - h^2}$. Selected arbitrary ground range resolution δ_g , we can calculate the intensity for each ground range interval as a weighted sum of the corresponding bins.

Note that by selecting $\theta_0 = 30^\circ$, the removal of the nadir zone backscatter intensities, or the intensities in regions where no seafloor is detected, is performed implicitly for our data, see example in Fig. 5. The choice of θ_0 is dependent on the sensor as well as the mounting angle.

IV. EXPERIMENTAL RESULTS

A. Data Preparation

The dataset we use in this project was collected in a survey of a fjord by a Kongsberg Hugin AUV equipped with EM2040 Multibeam and Edgetech 2205 sidescan sonars. By conducting the *sidescan draping* process described in [25], bathymetry built from MBES data can associate the intensity for each bin to its georeferenced coordinates, which finds the potential pixel correspondences between SSS images automatically. Manual correction is later conducted to adjust the keypoint positions to register a correspondence.

Given the annotated correspondences as ground truth reference, patch pairs are extracted from SSS images for the evaluation of the canonical transformation. The first step is to split the anchor waterfall image into starboard and port sides, since distance between pixels in two sides would not reflect real geometry after nadir zone removal. For each side, keypoint sets are selected in a constant size of ping set. In each pair of SSS images, patches are extracted around the corresponding keypoint sets in the same window sizes. An example of extracted patch pair in raw and canonical images is displayed in Fig. 4. Eventually a dataset with 1270 keypoint correspondences along 13208 pings and 60 patch pairs was created.

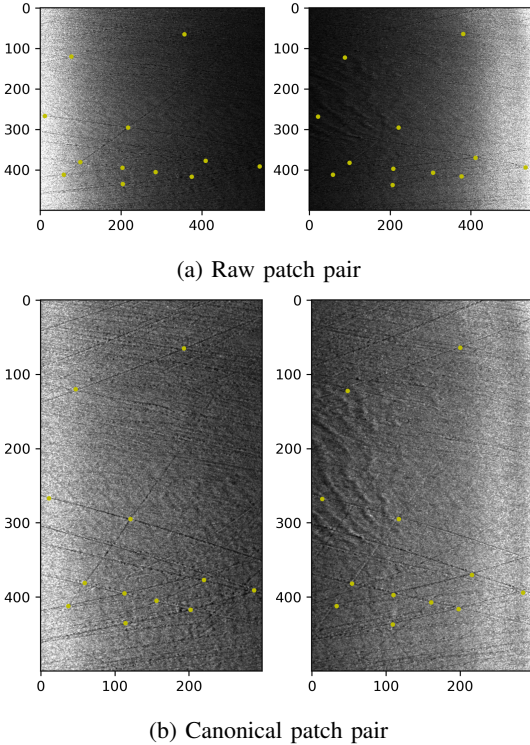


Fig. 4: Example patch pair extracted from two SSS images. (a) and (b) represents the same patches in raw and canonical images, respectively. The annotated keypoints are marked by the yellow dots.

B. Evaluation Metrics

To evaluate the effect of canonical transformation, two types of metrics are applied. One is intensity based methods including correlation measure and histogram distance between a patch pair to reflect the patch similarity. The other is descriptor based method evaluating the matching accuracy of keypoints between SSS images. For both metrics the baseline is computed using the patch pairs extracted from raw SSS images.

Correlation measure is usually applied to conduct pixel level comparison of two images of the same object taken in different time. Given $F(x, y)$ and $G(x, y)$ which represent the intensity in the same location (x, y) of patches F and G , the normalized correlation of the two patches is:

$$R(F, G) = \frac{\sum_{x,y} (F(x, y) \cdot G(x, y))}{\sqrt{\sum_{x,y} F(x, y)^2 \cdot \sum_{x,y} G(x, y)^2}}. \quad (6)$$

The range of correlation is in $[0, 1]$, with a higher score indicating a better similarity between the evaluated patches.

As pixel level offset exists during manual keypoint annotation, two histogram distance metrics, Kullback-Leibler divergence [26] and Chi-square distance [27], are proposed as additional measures to improve robustness in patch similarity evaluation. Given the histograms of patch pairs H_1 and H_2 along the same bin range, the Kullback-Leibler divergence is:

$$d_{KL}(H_1, H_2) = \sum_I H_1(I) \log \left(\frac{H_1(I)}{H_2(I)} \right), \quad (7)$$

and the Chi-square distance is:

$$d_C(H_1, H_2) = 2 \sum_I \left(\frac{(H_1(I) - H_2(I))^2}{H_1(I) + H_2(I)} \right). \quad (8)$$

For both distances, a higher returned score represents increasing dissimilarity between the patch pair.

For descriptor based evaluation, we extract two representative hand-crafted descriptors, ORB [28] and SIFT [29], at the annotated keypoints of each patch pair, and match them between the patch by comparing their descriptor distances. The accuracy of the found matches serves as metric.

C. Qualitative Results

An intuitive comparison of each step in the canonical transformation using the \cos^2 Lambertian law is demonstrated in Fig. 5. In the raw image in Fig. 5a, the center part of the image (regions closed to the nadir of the SSS) shows much stronger backscatter intensity compared to the far edges of the image. When visualizing the entire SSS image as a whole, this leads to information loss in both regions. Fig. 5b shows that beam pattern correction results in minor improvements. More significant improvement is seen in Fig. 5c when intensity correction is applied. As the central areas with high echo intensities are normalized by reducing the \cos^2 Lambertian law, the intensities over the whole image look more even along swaths, which leads to a wider dynamic range for areas with useful information. In Fig. 5c, a feature close to nadir in one

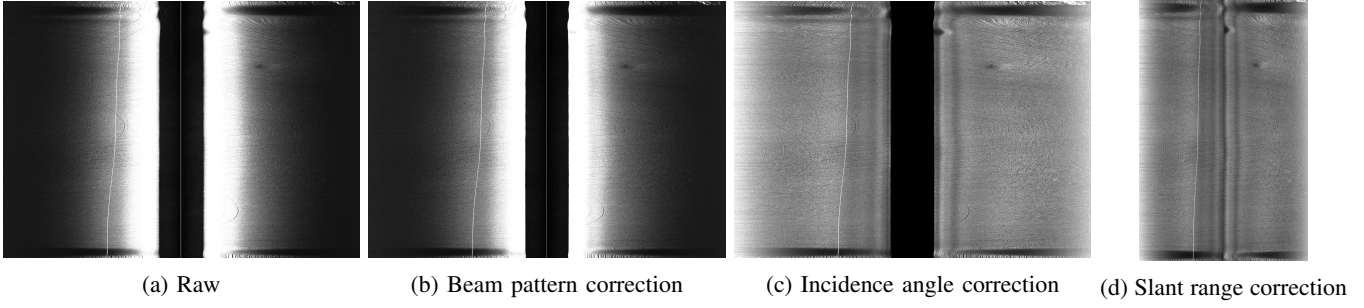


Fig. 5: Comparison of a SSS waterfall image after each of the proposed transformation steps using \cos^2 law. (a)-(d) corresponds to the output after each step of the transformation, where (a) is the raw image, (b) is the beam pattern correction result, (c) is the incidence angle correction result and (d) is the slant range correction result, which is also the final output the proposed canonical transformation. The black strip in the center of (a)-(c) is the *nadir zone* with low backscatter intensity and represents the distances where no seafloor is detected by the SSS. This region is removed in (d).

image and far from the nadir in another image have more similar range of intensities. Fig. 5d shows the final result after slant range correction, where the nadir zone in the center is removed and the image appears to have more even scale.

Fig. 1 gives a closer inspection on effect of slant range correction on a feature's size. In Fig. 1, four keypoints are placed in the feature consisting of two curves, and a red rectangle is drawn to visualize the total area covered by these keypoints. In the raw patch pair, the window size is 112×194 and 153×197 , respectively. The increasing width in raw patches demonstrates that the same feature covers more bins as it moves away from the nadir. In the canonical patches, the window size is 78×194 and 77×197 , respectively. This indicates that the canonical transformation significantly improves the consistence of a feature's size in different ranges from the nadir by spacing bins uniformly along the ground range.

D. Quantitative Results

1) *Correlation Measure*: Here we compute the correlation similarity between the 60 patch pairs in our dataset. For each canonical transformation method, the improvement in correlation is computed as $\rho = \frac{\bar{R} - R}{R}$, with R being the score on raw images and \bar{R} the score on canonical images. Table I shows the performance of raw and canonical patch pairs. All of the tested canonical transformations improved the correlation of 98.33% of the patches, i.e. only 1 of the 60 patch pairs did not see improvement in correlation. Among them, the \cos^2 law achieved the highest performance, improving the average correlation from 0.6905 by 34.50% to 0.9287.

TABLE I: Results in correlation measure for raw and canonical dataset. The highest values are highlighted in **bold**.

Method	Proportion of Improved patches	Average Similarity	Average Improvement
None	—	0.6905	—
cos	98.33%	0.8810	27.59%
\cos^2	98.33%	0.9287	34.50%
cot	98.33%	0.8988	30.17%

2) *Histogram Distance*: The result of histogram evaluations is listed in Table II. For each distance metric we analyse the proportion of improved patches after canonical transformation and average decrease $\rho = \frac{d - \bar{d}}{\bar{d}}$ using the average original distance d and canonical distance \bar{d} . The canonical transformation with \cos^2 law again reaches the overall best performance in both metrics, with the average histogram distances in both metrics decreased by around 40%, and proportion of improved patches being 91.67% and 83.33%, respectively.

TABLE II: Results in histogram distance measure for raw and canonical dataset. The best values for each distance metric are highlighted in **bold**.

Distance metric	Method	Proportion of improved patches	Average score	Average decrease
Chi-square	None	—	485.37	—
	cos	93.33%	339.72	30.01%
	\cos^2	91.67%	298.59	38.48%
	cot	95.00%	326.56	32.72%
KL-divergence	None	—	1993.36	—
	cos	70.00%	1586.12	20.43%
	\cos^2	83.33%	1226.24	38.48%
	cot	75.00%	1483.33	25.59%

3) *Descriptor Matching*: Table III shows the descriptor matching results with the total number of proposed matches, the number of correct matches and the matching accuracy. For SIFT descriptors, all three tested canonical transformations lead to increase in number of total and correct matches, as well as higher matching accuracy. The best performance is again found using the \cos^2 Lambertian law with a final matching accuracy of 92.68%, which is a slight improvement ($\approx 5\%$) from the raw case. For ORB descriptors, the result is less conclusive. Out of the three canonical transformation cases, only \cos^2 resulted in improved matching accuracy. It is also evident from Table III that out of the two tested descriptors, SIFT obtain both higher number of matches and higher accuracy and is more suitable for feature extraction from SSS images.

However, due to the limited number of image patches used for evaluation, definite conclusions on the effect of canonical

TABLE III: Matching results of ORB and SIFT descriptors for raw and canonical transformation. The best values for each distance metric are highlighted in **bold**.

Descriptors	Method	Total Matches	Correct Matches	Accuracy
SIFT	None	153	133	86.93%
	cos	160	146	91.25%
	\cos^2	164	152	92.68%
	cot	168	151	89.88%
ORB	None	75	50	66.67%
	cos	87	55	63.22%
	\cos^2	76	54	71.05%
	cot	85	55	64.71%

transformation on descriptor matching performance cannot be drawn. Instead, we look for specific instances where canonical respective raw images achieve higher descriptor matching accuracy and analyse the qualitative differences between image patches. This analysis is only performed for SIFT descriptors due to its higher overall accuracy.

Fig. 6 shows the correct number of matches proposed by SIFT across all patch pairs in the dataset, grouped by the survey line pairs where the patches are extracted from. The structure of the plot suggests that the performance of SIFT descriptors is indeed survey line dependent. For specific analysis, Fig. 7 is an example from survey line pair *ssh172-ssh171*, where the number of correct SIFT descriptor matches on the raw image outperforms that on all three canonical images. Fig. 8 provides an opposite example from survey line pair *ssh172-ssh170*, where SIFT obtained higher number of correct matches on all canonical images compared to on the raw image.

In Fig. 7, the two raw image patches both show significant but similar, intensity distortions compared to the canonical ones. This might be why the canonical transformation does not help.

In Fig. 8, the left image patch is extracted from closer to the nadir region, whilst the right image patch is extracted around the center. This makes the distortions in the raw image quite different in the two. Thus removing the distortions is more helpful.

From these examples, we hypothesise that the proposed canonical transformation can help preserve the repeatability of descriptors for keypoints lying in regions with large geometric and intensity distortions, though more extensive experiments are required for any conclusive results.

4) *Discussion:* The proposed canonical representation achieves great performance in intensity based metric, including correlation measure and two histogram distances. The results suggest that the \cos^2 law achieves the best performance in increasing the similarity of patch pairs. For descriptor evaluations, the canonical transformation with \cos^2 Lambertian law can improve the matching accuracy for both SIFT and ORB descriptors by a small amount, as shown in Table III. However, the improvement is not consistent across all image pairs and more experiments should be conducted before any conclusive results can be drawn.

Since most significant improvement is found in patch simi-

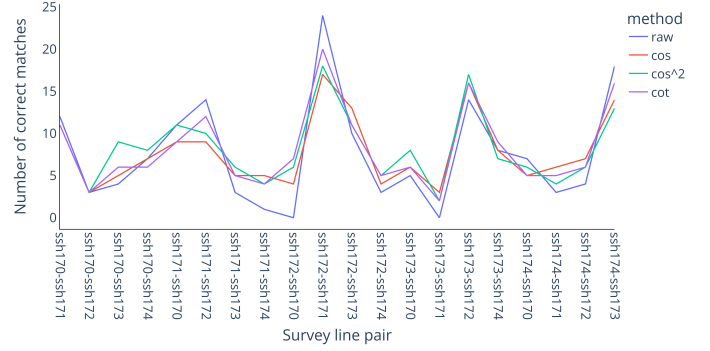


Fig. 6: Correct number of matches found by using SIFT descriptor between all survey line pairs in the dataset.

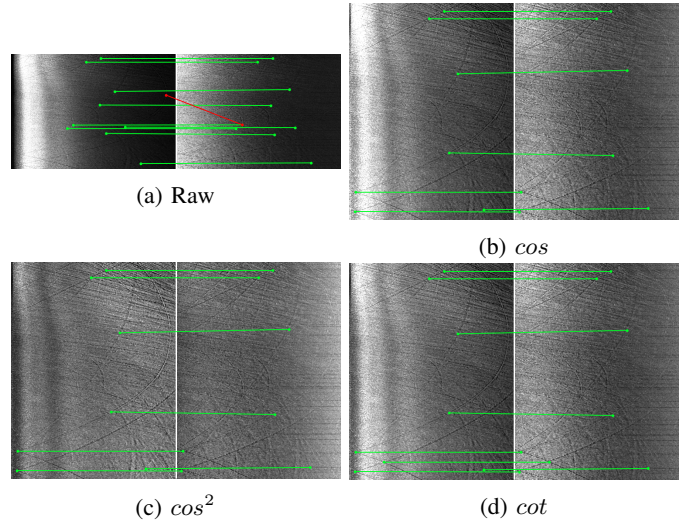


Fig. 7: Example patch from the survey line pair *ssh172-ssh171*, where the SIFT descriptor matching results on the raw image outperformed that on all three canonical images. The green and red lines indicate correctly and incorrectly proposed matches, respectively. In this example, the number of correct matches found in the raw image (a) is larger than in any other canonical images (b-d). One erroneous match is found in the raw image (a) and no erroneous matches are found in the canonical images (b-d).

larity, our method is perhaps more suitable for tasks requiring canonical shape of patches for data associations, for instance, dense patch matching [30], [31], which would be an interesting future direction. Furthermore, the proposed canonical transformation could be applied as a preprocessing step for other downstream tasks, such as place recognition using SSS images [18], which is useful for loop closure detection in SSS SLAM.

V. CONCLUSION

In this paper we present a canonical transformation method for side-scan sonar. The proposed method is carefully evaluated on real data with annotated keypoints as ground truth,

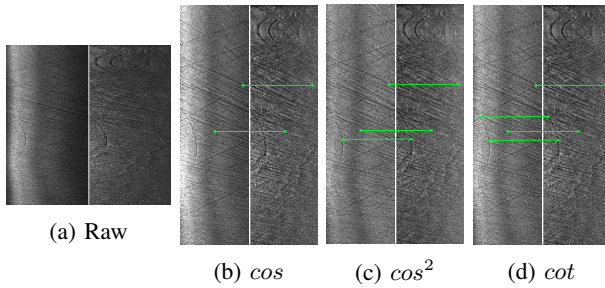


Fig. 8: Example patch from the survey line pair *ssh172-ssh170*, where the SIFT descriptor matching on all three canonical images outperformed that on the raw image. The green and red lines indicate correctly and incorrectly proposed matches, respectively. In this example, no matches is proposed in the raw image (a), and only correct matches have been proposed by the canonical images (b-d).

using two types of metrics. We have shown that canonical transformations of SSS image can lead to better patch similarity and descriptor matching accuracy, with the transformation using \cos^2 Lambertian law achieving the overall highest performance.

To guide future work, one could speculate that the proposed method could help enrich the data for training of neural networks by uniforming the SSS images from different locations (e.g. varying altitudes). The proposed method could also be helpful to other feature-based tasks such as object detection and sparse keypoint matching, as well as patch-based tasks such as loop closure detection for SSS SLAM, and dense patch matching for SSS image registration and mosaicking, etc.

ACKNOWLEDGMENT

This work was partially supported by the Wallenberg AI, Autonomous Systems and Software Program (WASP) funded by the Knut and Alice Wallenberg Foundation and partially supported by Stiftelsen för Strategisk Forskning (SSF) through the Swedish Maritime Robotics Centre (SMaRC) (IRC15-0046).

REFERENCES

- [1] S. Thrun, "Probabilistic robotics," *Communications of the ACM*, vol. 45, no. 3, pp. 52–57, 2002.
- [2] K. Köser and U. Frese, "Challenges in underwater visual navigation and slam," in *AI Technology for Underwater Robots*. Springer, 2020, pp. 125–135.
- [3] I. Torroba, N. Bore, and J. Folkesson, "Towards autonomous industrial-scale bathymetric surveying," in *2019 IEEE/RSJ International Conference on Intelligent Robots and Systems (IROS)*. IEEE, 2019, pp. 6377–6382.
- [4] K. Siantidis, "Side scan sonar based onboard slam system for autonomous underwater vehicles," in *2016 IEEE/OES Autonomous Underwater Vehicles (AUV)*. IEEE, 2016, pp. 195–200.
- [5] P. Blondel, *The Handbook of Sidescan Sonar*, 2009.
- [6] A. Burguera and G. Oliver, "Intensity correction of side-scan sonar images," in *Proceedings of the 2014 IEEE Emerging Technology and Factory Automation (ETFA)*. IEEE, 2014, pp. 1–4.
- [7] D. T. Cobra, A. V. Oppenheim, and J. S. Jaffe, "Geometric distortions in side-scan sonar images: A procedure for their estimation and correction," *IEEE Journal of oceanic engineering*, vol. 17, no. 3, pp. 252–268, 1992.

- [8] P. S. Chavez Jr, J. Isbrecht, P. Galanis, G. L. Gabel, S. C. Sides, D. L. Soltesz, S. L. Ross, and M. G. Velasco, "Processing, mosaicking and management of the monterey bay digital sidescan-sonar images," *Marine Geology*, vol. 181, no. 1-3, pp. 305–315, 2002.
- [9] A. Burguera and G. Oliver, "High-resolution underwater mapping using side-scan sonar," *PloS one*, vol. 11, no. 1, p. e0146396, 2016.
- [10] J. Zhao, J. Yan, H. Zhang, and J. Meng, "A new radiometric correction method for side-scan sonar images in consideration of seabed sediment variation," *Remote Sensing*, vol. 9, no. 6, p. 575, 2017.
- [11] C. Capus, I. T. Ruiz, and Y. Petillot, "Compensation for changing beam pattern and residual tvg effects with sonar altitude variation for sidescan mosaicking and classification," in *7th. Eur. Conf. Underwater Acoustics, Delft, The Netherlands*, vol. 1, 2004.
- [12] S. Reed, I. T. Ruiz, C. Capus, and Y. Petillot, "The fusion of large scale classified side-scan sonar image mosaics," *IEEE transactions on image processing*, vol. 15, no. 7, pp. 2049–2060, 2006.
- [13] C. Peng, S. Fan, X. Cheng, Y. Cao, and G. Zeng, "An improved side scan sonar image processing framework for autonomous underwater vehicle navigation," in *Proceedings of the 15th International Conference on Underwater Networks & Systems*, 2021, pp. 1–5.
- [14] J. Zhang, Y. Xie, L. Ling, and J. Folkesson, "A fully-automatic side-scan sonar slam framework," *arXiv preprint arXiv:2304.01854*, 2023.
- [15] A. Burguera and F. Bonin-Font, "On-line multi-class segmentation of side-scan sonar imagery using an autonomous underwater vehicle," *Journal of Marine Science and Engineering*, vol. 8, no. 8, p. 557, 2020.
- [16] P. Vandrish, A. Vardy, D. Walker, and O. Dobre, "Side-scan sonar image registration for auv navigation," in *2011 IEEE Symposium on Underwater Technology and Workshop on Scientific Use of Submarine Cables and Related Technologies*. IEEE, 2011, pp. 1–7.
- [17] P. King, B. Anstey, and A. Vardy, "Comparison of feature detection techniques for auv navigation along a trained route," in *2013 OCEANS - San Diego*, 2013, pp. 1–8.
- [18] M. Larsson, N. Bore, and J. Folkesson, "Latent space metric learning for sidescan sonar place recognition," in *2020 IEEE/OES Autonomous Underwater Vehicles Symposium (AUV)*. IEEE, 2020, pp. 1–6.
- [19] E. Coiras, Y. Petillot, and D. M. Lane, "Multiresolution 3-d reconstruction from side-scan sonar images," *IEEE Transactions on Image Processing*, vol. 16, no. 2, pp. 382–390, 2007.
- [20] Y. Xie, N. Bore, and J. Folkesson, "Towards differentiable rendering for sidescan sonar imagery," in *2022 IEEE/OES Autonomous Underwater Vehicles Symposium (AUV)*. IEEE, 2022, pp. 1–6.
- [21] M. D. Aykin and S. Negahdaripour, "Forward-look 2-d sonar image formation and 3-d reconstruction," in *2013 OCEANS-San Diego*. IEEE, 2013, pp. 1–10.
- [22] E. I. Thorsos, K. L. Williams, N. P. Chotiros, J. T. Christoff, K. W. Commander, C. F. Greenlaw, D. V. Holliday, D. R. Jackson, J. L. Lopes, D. E. McGehee *et al.*, "An overview of sax99: Acoustic measurements," *IEEE Journal of Oceanic Engineering*, vol. 26, no. 1, pp. 4–25, 2001.
- [23] J. Folkesson, H. Chang, and N. Bore, "Lambert's cosine law and sidescan sonar modeling," in *2020 IEEE/OES Autonomous Underwater Vehicles Symposium (AUV)*. IEEE, 2020, pp. 1–6.
- [24] W. Xu, "Pixel correspondences for slam using sidescan sonar with canonical representations," 2022.
- [25] N. Bore and J. Folkesson, "Modeling and simulation of sidescan using conditional generative adversarial network," *IEEE Journal of Oceanic Engineering*, vol. 46, no. 1, pp. 195–205, 2020.
- [26] I. Csizsár, "I-divergence geometry of probability distributions and minimization problems," *The annals of probability*, pp. 146–158, 1975.
- [27] J. Puzicha, T. Hofmann, and J. M. Buhmann, "Non-parametric similarity measures for unsupervised texture segmentation and image retrieval," in *Proceedings of IEEE Computer Society Conference on Computer Vision and Pattern Recognition*. IEEE, 1997, pp. 267–272.
- [28] E. Rublee, V. Rabaud, K. Konolige, and G. Bradski, "Orb: An efficient alternative to sift or surf," in *2011 International conference on computer vision*. Ieee, 2011, pp. 2564–2571.
- [29] D. G. Lowe, "Distinctive image features from scale-invariant keypoints," *International journal of computer vision*, vol. 60, no. 2, pp. 91–110, 2004.
- [30] C. Barnes, E. Shechtman, A. Finkelstein, and D. B. Goldman, "Patch-match: A randomized correspondence algorithm for structural image editing," *ACM Trans. Graph.*, vol. 28, no. 3, p. 24, 2009.
- [31] S. Korman and S. Avidan, "Coherency sensitive hashing," *IEEE transactions on pattern analysis and machine intelligence*, vol. 38, no. 6, pp. 1099–1112, 2015.